Investigation of the fusion process for $^{10}B + ^{197}Au$ at near-barrier energies

M. Aversa,[1,2] D. Abriola,[1] M. A. G. Alvarez,[3] A. Arazi,[1,4] M. A. Cardona,[1,4] L. C. Chamon,[5] E. de Barbará,[1] J. de Jesús,[1] J. P. Fernández-García,[3,6] L. R. Gasques,[5] D. Hojman,[1,4] A. Lépine-Szily,[5] G. V. Martí,[1] A. J. Pacheco,[1,4] V. Scarduelli,[5] and V. A. B. Zagatto[7]

[1]*Laboratorio TANDAR, Comisión Nacional de Energía Atómica, Av. Gral. Paz 1499, BKNA1650 San Martín, Argentina*
[2]*Departamento de Física, FCEyN, Universidad de Buenos Aires, Pabellón 1, Ciudad Universitaria, 1428 Buenos Aires, Argentina*
[3]*Departamento FAMN, Universidad de Sevilla, Apartado 1065, 41080 Sevilla, Spain*
[4]*Consejo Nacional de Investigaciones Científicas y Técnicas, Av. Rivadavia 1917, C1033AAJ Buenos Aires, Argentina*
[5]*Universidade de Sao Paulo, Instituto de Fisica, Rua do Matao, 1371, 05508-090, Sao Paulo, SP, Brazil*
[6]*Centro Nacional de Aceleradores, Universidad de Sevilla, Junta de Andalucía-CSIC, 41092 Sevilla, Spain*
[7]*Instituto de Física da Universidade Federal Fluminense, 24210-346, Niterói, Rio de Janeiro, Brazil*

(Received 5 February 2020; accepted 2 March 2020; published 1 April 2020)

In a previous work, we presented data for the $^{10}B + ^{197}Au$ system, corresponding to quasielastic and elastic scattering, ^{197}Au inelastic excitation, and one neutron pickup transfer, measuring the angular distribution of scattered beam-like ejectiles at several energies around the Coulomb barrier. In this paper, we present data for the fusion process of the same system, at several energies around the Coulomb barrier, as well as new data for one neutron pickup and stripping transfer. In this case, we detected offline γ rays stemming from the β-delayed decay chain of fusion-evaporation residues and heavy transfer products. As in our previous work, we analyzed this data set with coupled reaction channels calculations using the São Paulo potential. We show that the coupling to the one neutron transfer channel is quite important to describe the fusion data at the sub-barrier energy region. We also provide a comparison of the experimental fusion cross sections obtained for $^{10}B + ^{197}Au$ with data for several other systems involving the same target nucleus.

DOI: 10.1103/PhysRevC.101.044601

I. INTRODUCTION

Several models for the real and imaginary parts of the nuclear interaction potential have been developed to describe a large number of heavy-ion elastic scattering data measured at energies below and above the Coulomb barrier [1–7]. Although the elastic scattering represents the most direct and simplest process concerning a nuclear reaction, its description can become extremely challenging if the effect of couplings to nonelastic channels is strong. Particularly, in nuclear collisions involving weakly bound or radioactive nuclei, direct processes, such as transfer or breakup, can affect the dynamics of the reaction due to their cluster structure and low breakup energy threshold [8–15].

The breakup effects of weakly bound nuclei on different reaction channels has been extensively investigated. In particular, the influence of breakup on the fusion mechanism has attracted considerable attention in the last years. Several experiments have been performed using different techniques, where both complete fusion (CF) cross sections (occurring when the whole projectile fuses with the target) and incomplete fusion (ICF) cross sections (occurring when at least one of the fragments is absorbed by the target) were determined. The sum of CF and ICF is called total fusion (TF). Generally, a suppression of the experimental CF cross sections at energies above the Coulomb barrier is observed in comparison with results obtained from single barrier penetration model calculations [16–19]. This phenomenon is associated with the typically low breakup threshold of the weakly bound projectiles, which may break up into a number of different mass partitions before reaching the fusion barrier.

Among the weakly bound stable nuclei, the ^{10}B nucleus presents a $^{6}Li + \alpha$ cluster structure with a fairly low threshold of 4.46 MeV. In a recent work [20], we presented data for various reaction channels relative to the $^{10}B + ^{197}Au$ collision at several energies around the Coulomb barrier. The data set included elastic and quasielastic scattering, ^{197}Au inelastic excitation, one neutron pickup transfer, and ^{9}Be detection, that we have associated to one-proton stripping transfer and breakup. The data have been obtained in two laboratories: the Open Laboratory of Nuclear Physics (LAFN, acronym in Portuguese) in Brazil, and the TANDAR Laboratory in Argentina. This complete data set was well described through theoretical coupled reaction channels (CRC) calculations which showed the importance of these couplings to describe experimental data.

In this work, we present new experimental data for the total fusion (TF) cross sections for the $^{10}B + ^{197}Au$ system obtained at the TANDAR Laboratory from offline measurements of the characteristic γ-ray yields. The paper is organized as follows. Experimental details of fusion and n-transfer cross section measurements are given in Sec. II. CRC calculations of the fusion excitation function for $^{10}B + ^{197}Au$ and a comparison with data for other systems involving the same target

nucleus are presented in Sec. III. A summary of the main results and conclusions is given in Sec. IV.

II. EXPERIMENTAL SETUP AND PROCEDURES

^{10}B beams were extracted from cathodes with enriched material and accelerated to laboratory energies between 38 MeV and 61 MeV by the 20 UD TANDAR Accelerator, operating at terminal voltages up to 10 MV. These beams, with typical intensities around 10 pnA, impinged on ^{197}Au target foils with approximated thicknesses of 250 μg/cm^2, placed in a 70 cm diameter scattering chamber. Two monitor detectors, placed at $+16^\circ$ and -16° from the beam direction, and a Faraday cup were used for normalization purposes. During these irradiations, a set of ten silicon detectors measured the quasielastic angular distributions. These results were presented in our previous work [20].

Aluminum foils with 200 μg/cm^2 thickness were placed 1 mm behind the targets to act as catchers for transfer recoils and fusion products from the ^{10}B + ^{197}Au reaction that were not retained within the gold target. The catcher thickness allowed the beam and beam-like ejectiles to pass through it and be detected by the Faraday cup and silicon detectors. The ^{10}B + ^{27}Al fusion products, much lighter than those from ^{197}Au, were also not retained in the catcher foil. The energy losses were less than 250 keV in the ^{197}Au target (this defines the maximal spread in the reaction energy for each measurement) and less than 350 keV in the ^{27}Al catcher. The energy straggling due to the target and catcher was about 30 keV, which assures that the monitor detectors can resolve particles elastically scattered at the ^{197}Au target and at the ^{27}Al catcher. Aluminum was chosen as catcher material because all fusion-evaporation products of the ^{10}B + ^{27}Al reaction are very short-lived (few seconds) and, hence, produce almost no interfering γ rays during the offline measurement.

For each bombarding energy, a new set of target and catcher foils was used. Although requiring one irradiation for each incident beam energy, this experimental setup, using relatively thin targets and catchers, provides a much better energy resolution, as well as an improved peak to background ratio, compared to the stack-foil method. The targets were irradiated between 5 to 9 h, according to the available beam intensity and the expected amount of events for each channel. To record the time profile of the beam intensity, elastic events on both monitors and events from the Faraday cup integrator were recorded each second. Nevertheless, for the derivation of cross sections values, time bins between 1 and 10 min were used. Within 15 min after the end of the activation, target and catcher foils were removed through an extraction capsule, keeping the vacuum in the scattering chamber, and placed at a fixed distance from a 40% efficiency high-purity germanium (HPGe) detector (1.9 keV energy resolution at 1332 keV) shielded by a lead castle. There, the activity of each β-delayed γ ray was measured. Immediately after this, another 20% efficiency HPGe detector (3.4 keV energy resolution) was used for a second measurement. Finally, approximately a week later, the target and catcher were analyzed again in the first detector. These activity measurements lasted from 5 h to 3 d. The absolute efficiencies of the HPGe detectors were determined using ^{60}Co, ^{133}Ba, ^{137}Cs, and ^{152}Eu calibrated γ sources.

TABLE I. Main output channels from the n-transfer and fusion-evaporation processes for the ^{10}B + ^{197}Au reaction. Reaction Q values, decay processes, half-lives ($T_{1/2}$), main γ-ray energies, and intensities are quoted. (^{6}Li, xn) stand for the ICF following ^{10}B $\rightarrow$ ^{6}Li + α breakup.

Channel	Q (MeV)	Decay	$T_{1/2}$	E_γ (kev)	I_γ (%)
		n-transfer			
(^{10}B, ^{9}B)	−1.9	^{198}Au → ^{198}Hg	2.7 d	411.8	96
(^{10}B, ^{11}B)	3.4	^{196}Au → ^{196}Hg	6.2 d	355.7	87
				333.0	23
		fusion-evaporation:			
(^{10}B, 3n)	−25.0	^{204}Po → ^{204}Bi	3.5 h	884.0	34
				270.1	32
				1016.3	28
(^{10}B, 4n)	−34.1	^{203}Po → ^{203}Bi	37 min	908.6	55
				1090.9	19
				893.5	19
(^{10}B, 5n)	−41.5	^{202}Po → ^{202}Bi	45 min	688.8	100
				316.1	28
				165.8	17
(^{10}B, 2np)	−21.9	^{204}Bi → ^{204}Pb	11.22 h	899.2	99
				374.8	83
				984.0	60
(^{10}B, 3np)	−29.1	^{203}Bi → ^{203}Pb	11.76 h	820.2	30
				825.2	15
				896.9	13
(^{10}B, 4np)	−37.9	^{202}Bi → ^{202}Pb	1.71 h	960.7	99
				422.1	84
				657.5	61
(^{10}B, 2$n\alpha$)	−12.3	^{201}Pb → ^{201}Tl	9.33 h	331.2	77
(^{6}Li, 2n)	−7.9				
(^{10}B, 3$n\alpha$)	−19.5	^{200}Pb → ^{200}Tl	21.5 h	147.6	38
(^{6}Li, 3n)	−15.0				
(^{10}B, 4$n\alpha$)	−28.6	^{199}Pb → ^{199}Tl	90 min	366.9	44
(^{6}Li, 4n)	−24.1				

Preliminary calculations using the PACE4 [21] statistical code for the fusion-evaporation process have been performed to determine the main output channels that could be expected for each bombarding energy. In Table I, the more intense γ rays corresponding to each expected output channel are listed [22–29].

The fusion of ^{10}B + ^{197}Au produces the proton-rich ^{207}Po compound nucleus, and later Po isotopes are produced by neutron evaporation. The offline detection of β-delayed γ rays is only sensitive to short-lived nuclei. In the present experiment, $^{202–204}$Po, $^{202–204}$Bi, $^{198–201,203}$Pb, $^{198–200}$Tl, and ^{196,198}Au nuclei, with half-lives from 30 min to 6 d, could be identified. ^{202}Pb, with a half-life of 52.5 ky, could not be detected.

In Fig. 1 a typical γ ray spectrum obtained for a bombarding energy of 55 MeV is shown. Each peak is identified by its energy and its parent nucleus, which belongs to the

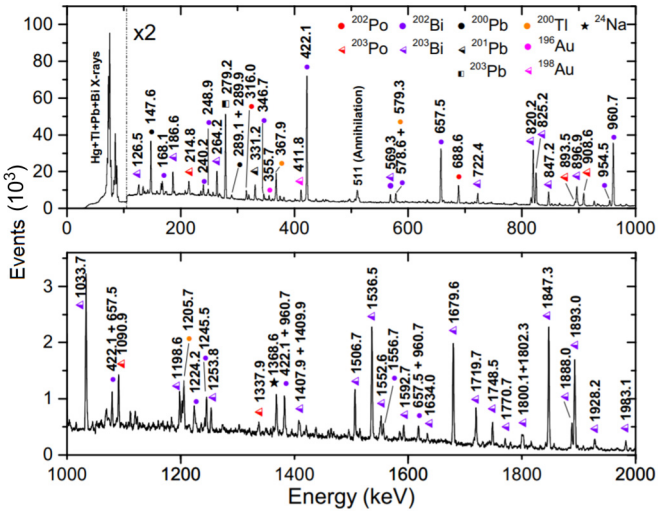

FIG. 1. Cutout of the γ ray spectrum obtained from the target and catcher foils with a 40% efficiency HPGe detector after the irradiation at a bombarding energy of 55 MeV. Peaks are identified by its parent nucleus. Peaks stemming from other identified parents (^{204}Po, ^{204}Bi, ^{198,199}Pb, ^{198,199}Tl) are not labeled for clarity.

β-delayed decay chain of different output channels (CF, ICF, and transfer) following the $^{10}\mathrm{B} + {}^{197}\mathrm{Au}$ reaction. γ events from the ^{24}Na decay (presumably produced by the $^{27}\mathrm{Al}(^{10}\mathrm{B}, {}^{9}\mathrm{B}\,\alpha)\,{}^{24}\mathrm{Na}$ reaction in the catcher foil [30]) and the 511 keV annihilation peak were also observed.

Another criterion for identifying each produced nucleus is its half-life. Figure 2 shows the number of γ events detected as a function of time. For clarity, bins of 1 h are used in this plot. Po isotopes are produced solely by CF followed by evaporation of 3–5 neutrons. Experimental data fit

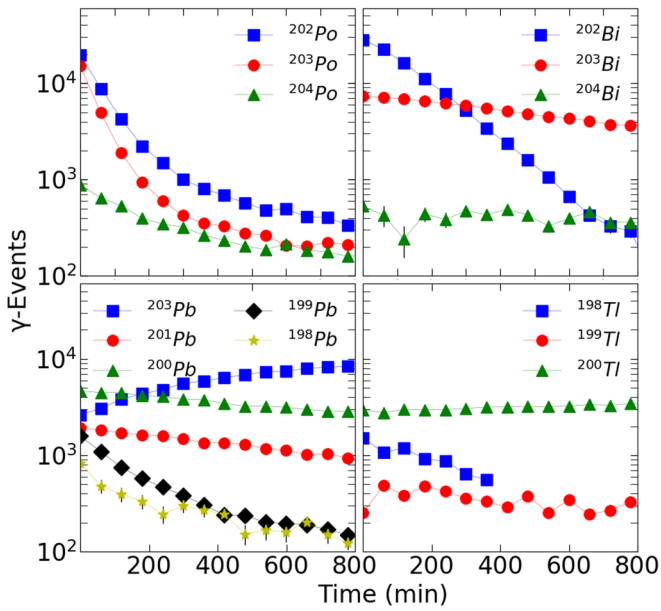

FIG. 2. Activity for main produced nuclides as a function of time. Except for ^{198}Tl, every nuclei activity was measured at bombarding energy 55 MeV. Solid lines are to guide the eye.

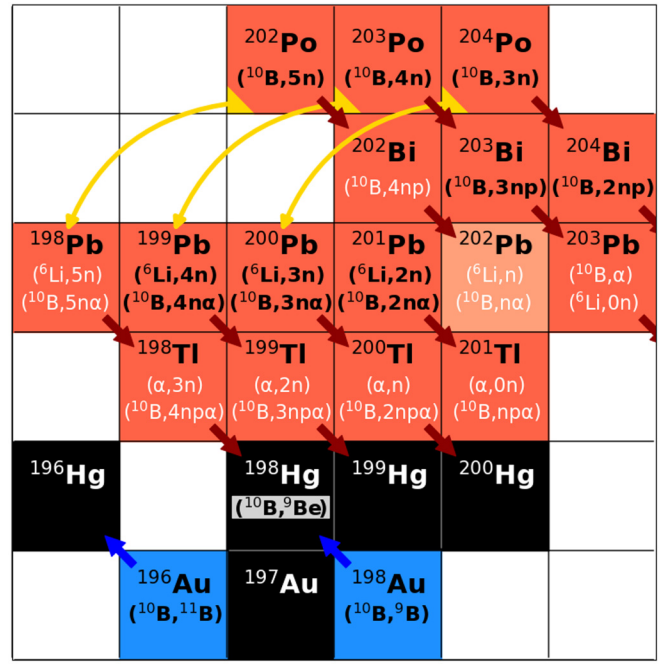

FIG. 3. Decay scheme of the identified nuclei in the γ spectrum. Stable nuclides are in black. Red, blue, and yellow colored nuclides and arrows represent β^+/electron capture, β^-, and α decay modes, respectively. ^{202}Pb, with a half-life too long to be detected (53 ky), is shown in light red. Possible production processes of each experimentally observed nuclide are indicated. Those written in white yielded a cross section compatible with zero. (^{6}Li, X) and (α, X) labels stand for the ICF following $^{10}\mathrm{B} \rightarrow {}^{6}\mathrm{Li} + \alpha$.

for ^{202}Po, ^{203}Po, and ^{204}Po decay curves (disregarding the last time bins in which the background dominates) yielded half-lives of (47.5 ± 0.8) min, (33.1 ± 0.4) min and (212 ± 10) min, in fair agreement with published values [22–24]. Note that nuclei fed by other decays (see Fig. 3) do not necessarily have a simple exponential decay. Bi isotopes are produced by the β^+ or electronic capture of Po isotopes or by evaporation of one proton and 2–4 neutrons from the ^{207}Po compound nucleus. In turn, Pb isotopes are produced either by the α decay of the Po isotopes, $xn\alpha$ evaporation of the ^{207}Po nucleus or ICF of $^{6}\mathrm{Li} + {}^{197}\mathrm{Au}$ followed by the evaporation of neutrons. Tl isotopes can stem from the β^+ or electronic capture of Pb isotopes, by the ICF $\alpha + {}^{197}$Au followed by the evaporation of neutrons or even by CF followed by evaporation of $xnp\alpha$. It is worth mentioning that the present experimental procedure does not allow the identification of different production mechanisms leading to the same nuclide.

γ rays from ^{196}Hg produced by the β^- decay of ^{196}Au and from ^{198}Hg produced by the β^- decay of ^{198}Au were identified in the spectra. These γ rays are associated with the neutron pickup and stripping processes, respectively. The β^+ decay of ^{198}Tl also produces ^{198}Hg nuclei, so their amount has been calculated and subtracted to get the $(^{10}\mathrm{B}, {}^{9}\mathrm{B})^{198}\mathrm{Au}$ cross section. Proton transfer processes produce either stable nuclides (^{198}Hg, ^{196}Pt, and ^{9}Be) or nuclides which do not produce γ radiation (^{11}C). Therefore, they could not be detected using the offline γ-ray technique.

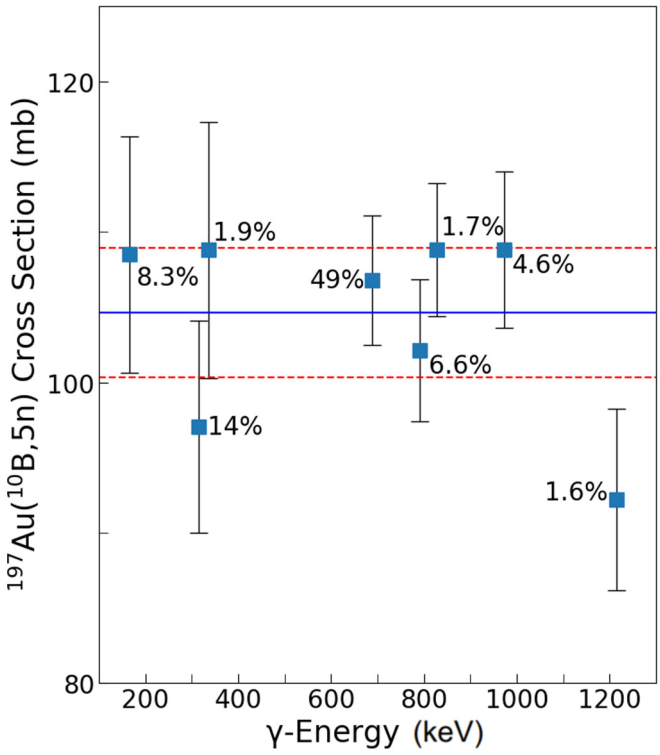

FIG. 4. Cross section of the ^{197}Au(^{10}B, $5n$) reaction for an energy of 55 MeV calculated through eight γ rays of the ^{202}Po β decay with different energies and relative intensities (indicated in the figure). Uncertainties of each cross section include the statistical components, background subtraction and detector efficiency uncertainty. Blue solid line is the weighted average and the red dashed lines its uncertainty.

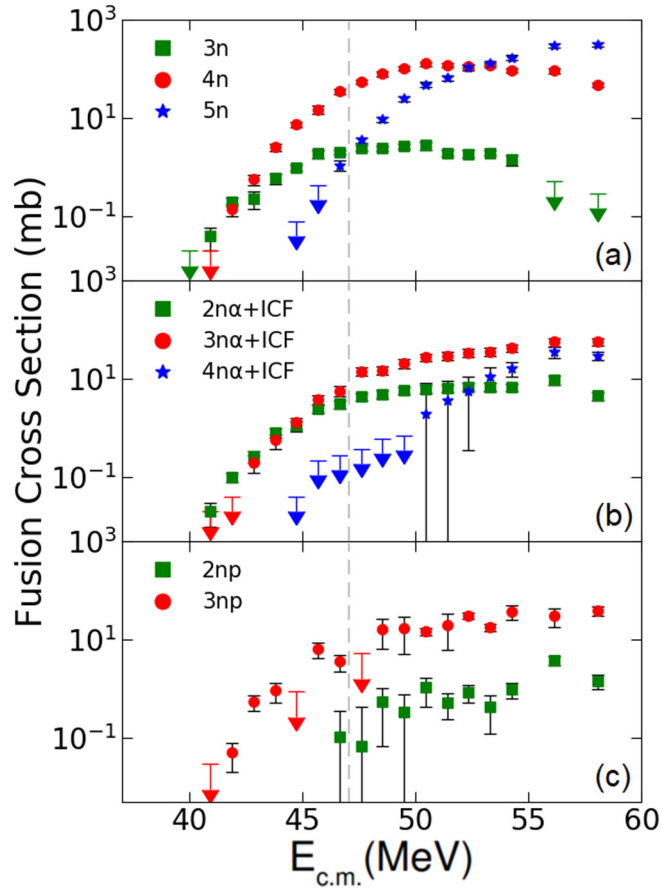

FIG. 5. Experimental cross sections (squares) and upper limits (arrows) to the observed channels. Cross sections for the formation of ^{204}Bi ($2np$), ^{203}Pb (α), and all Tl isotopes are compatible with zero. The vertical dashed line indicates the Coulomb barrier.

According to the half-life of each nuclide, a suitable time window was selected in order to maximize the peak to background ratio and, when possible, suppress the interference from overlapping peaks. The number of events in each peak ($N_{\rm ev}$) is obtained by fitting and integrating a Gaussian distribution. The number of background events $N_{\rm bg}$ was calculated as the average of the peak surroundings and subtracted from the gaussian peak. The cross section (σ) is calculated as

$$\sigma = \frac{(N_{\rm ev} - N_{\rm bg})\sigma_{\rm Ruth}}{\epsilon I e^{-\lambda t_0}(1 - e^{-\lambda \Delta t}) \int_0^{t_{\rm irr}} e^{\lambda t'} M(t') dt'}. \quad (1)$$

Here, $\lambda = \ln(2)/T_{1/2}$ is the nuclide decay constant, $t_{\rm irr}$ is the duration of the irradiation, t_0 is the measurement starting time, Δt is the measuring time, $M(t')$ is the number of elastic scattering events in the monitors per time unit, $\sigma_{\rm Ruth}$ is the corresponding Rutherford cross section, ϵ is the efficiency of each HPGe detector at the γ ray energy, and I is the relative intensity of the γ ray (see Table I). The integral accounts for the number of particles created in the irradiation and the exponential factor for their decay.

As an example, Fig. 4 shows the calculated cross section [according to Eq. (1)] for each γ ray stemming from the reaction ^{197}Au(^{10}B, $5n$) ^{202}Po process for an energy of 55 MeV. The blue solid line shows the weighted average (WA) which was adopted as experimental cross-section value. The dashed red lines indicate the uncertainty of the WA. The uncertainty finally reported (see Fig. 5) is the one of the WA, or the smaller uncertainty of individual measures, whichever is larger.

All experimental cross sections and some experimental upper limits are shown in Fig. 5, where each data point is the average of several peaks as explained before. Detailed data are available in Table I in the Supplemental Material [31]. Figure 5(a) shows the measured cross sections for the production of Po isotopes.

The detected amount of Bi, Pb, Tl isotopes can be larger than the amount of corresponding Po parents, since these isotopes, apart from being produced by the fusion mechanism can also be fed by β and α decays. Hence, the parent production has been subtracted from the yields of these isotopes. After this subtraction, cross sections for several processes (e.g., (^{10}B, $4np$, ^{202}Bi) turned to be compatible with zero (these processes are written in white in Fig. 3). In particular, ICF of $\alpha + {}^{197}$Au, leading to Tl isotopes, resulted in negligible cross sections. Similar results have been observed for the ^{10}B + ^{159}Tb reaction [18]. The direct production of Pb and Bi isotopes are shown in Figs. 5(b) and 5(c), respectively.

III. THEORETICAL CALCULATIONS

In the previous analysis of the quasi-elastic process for $^{10}B + ^{197}Au$ [20], the data were analyzed through theoretical CRC calculations using the FRESCO code [32]. The parameter-free São Paulo potential (SPP) [33] was adopted for the real part of the optical potential (OP), while the imaginary part was assumed as proportional to the SPP,

$$U_{OP}(R) = V_{SPP}(R) + i\,N_I\,V_{SPP}(R). \quad (2)$$

$N_I = 0.30$ was obtained as the value that provides the best data fit. A similar value ($N_I = 0.25$) has been obtained for the $^{10}B + ^{120}Sn$ system at energies around the corresponding Coulomb barrier [13,14]. We also included a real spin-orbit potential, related to the 3^+ ^{10}B ground state (g.s.), in the central part of the interaction, with form factor corresponding to a derivative of the Woods-Saxon shape. The respective reduced radius and diffuseness values were fixed: $r_0^{so} = 1.06$ fm and $a^{so} = 0.6$ fm. The data fit resulted in the $V_0^{so} = 6$ MeV strength value. In these conditions, a quite good theoretical description for the complete data set corresponding to the quasielastic, elastic, and inelastic scattering, and one-neutron pickup transfer, for several energies around the Coulomb barrier was obtained in [20]. Similar results have been obtained in the case of $^{10}B + ^{120}Sn$ [13,14].

The imaginary part of the OP of Eq. (2) involves internal as well as surface absorption, that we associate, respectively, to the fusion and also to some peripheral reaction processes that were not explicitly included in the CRC calculations. In the present work, we are just interested in the fusion process. Thus, the present CRC calculations were performed with an internal imaginary part for the OP, instead of that of Eq. (2). This imaginary part corresponds to a Woods-Saxon shape with a reduced radius $r_0 = 1.0$ fm, a diffuseness value $a = 0.30$ fm, and an imaginary depth $W_0 = 100$ MeV. All other parameter values, for the OP and couplings, were kept the same as in our previous quasielastic data analysis. Thus, we associate the theoretical fusion cross section to the flux absorbed by the internal OP imaginary part.

Before discussing fusion, in Fig. 6 we present experimental cross sections as a function of the energy for some peripheral reaction channels: (*i*) data for the $^{197}Au(^{10}B, ^{11}B)^{196}Au$ transfer reaction, obtained by the detection of the ^{11}B ejectiles with telescopes (ΔE-E) detectors (yellow circles); (*ii*) offline (β-delayed) γ detected from residual nuclei for $^{197}Au(^{10}B, ^{11}B)^{196}Au$ (black squares) and for $^{197}Au(^{10}B, ^{9}B)^{198}Au$ (red triangles). It is worthwhile to notice the good agreement between the results for the one neutron pickup obtained by different methods, the online detection of ^{11}B at the LAFN facility and the offline detection of ^{196}Au γ rays at the TANDAR Laboratory. The figure also presents CRC theoretical results for ^{197}Au inelastic scattering (solid blue line), as well as for one neutron pickup (dashed black line) and stripping transfer (dotted red line). Concerning the results for inelastic excitation, the calculations were performed considering only ^{197}Au states with excitation energies smaller than 600 keV (according to [20]).

As reported in [20], the data for one neutron pickup transfer correspond to integration over many ^{196}Au (and possibly also ^{11}B) states. Thus, in order to simulate this process within a simple approach, we performed CRC calculations considering only one ^{196}Au excited state, with excitation energy of 0.9 MeV and spin 1^- (which provided the best data fit for the angular distributions obtained at low energies [20]). The corresponding spectroscopic amplitude was considered as an adjustable parameter to fit the data. Since we deal just with a simulation with one single state, it is expected that the spectroscopic factor value is energy dependent. We have adopted similar procedure in the case of the one neutron stripping transfer. Since the Q value in this case is negative (and the Q optimum for neutron transfer is zero), the ^{198}Au g.s. was assumed as the only state involved in this simulation. In Fig. 7, we present the behaviors assumed for the spectroscopic amplitudes for one neutron stripping and pickup transfer as a function of the energy. The results shown in Fig. 6 represent

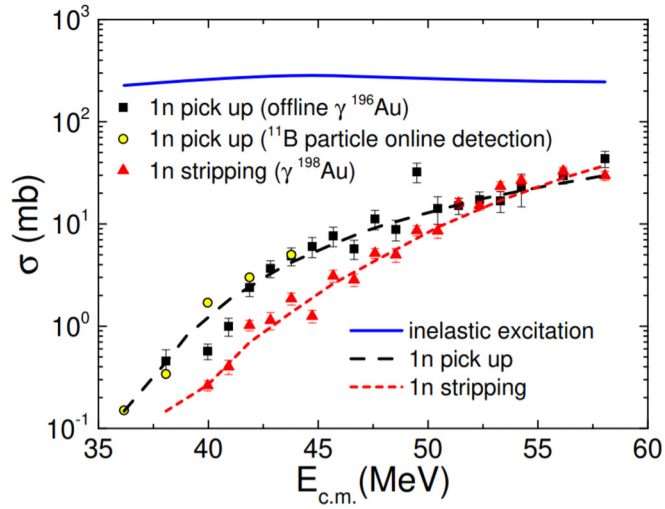

FIG. 6. Data and/or CRC theoretical results for ^{197}Au inelastic excitation (with $E^* \leqslant 600$ keV) and one neutron stripping and pickup transfer processes.

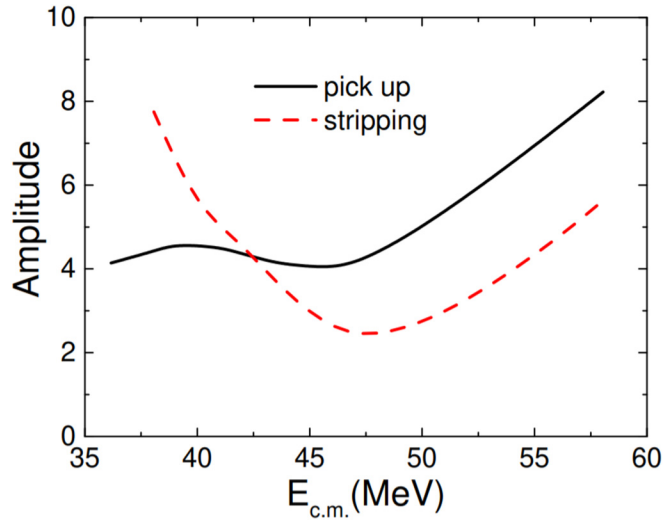

FIG. 7. Spectroscopic amplitudes as a function of the energy assumed for the one neutron pickup and stripping transfer processes.

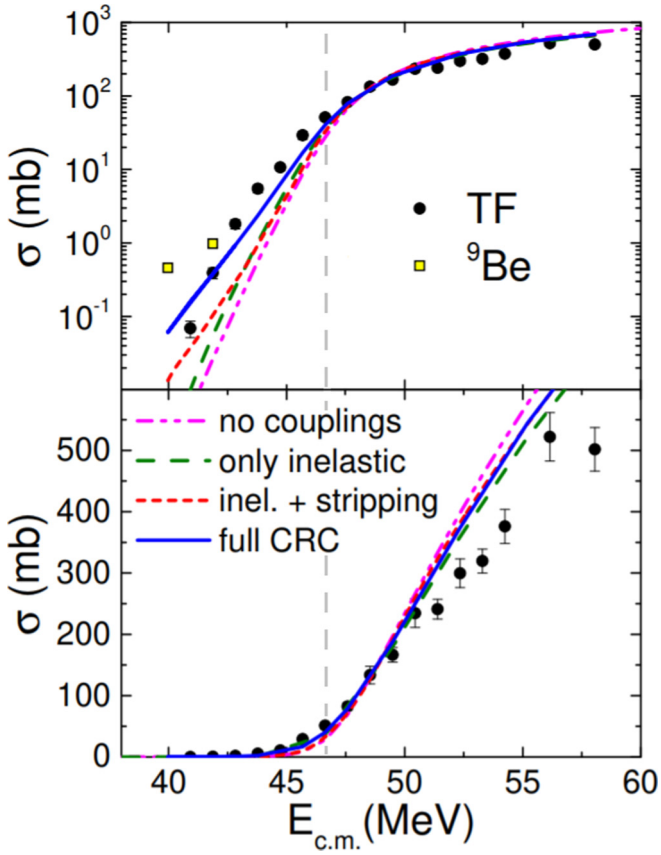

FIG. 8. Data for the total fusion (TF) process (black circles) as well as theoretical results considering different couplings in the CRC calculations. Yellow squares correspond to the detection of ^{9}Be reported in [20]. The vertical dashed line indicates the Coulomb barrier.

the respective CRC cross sections, which are in quite good agreement with the data. In this sense, we consider that we have performed realistic simulations for these couplings.

Data for fusion are presented in Fig. 8, in linear (bottom panel) and logarithmic (top) scales. The *s*-wave barrier height obtained with the SPP for this system is $V_B = 47.1$ MeV. The figure also presents theoretical cross sections obtained in different conditions: (*i*) no couplings; (*ii*) only couplings to inelastic states; (*iii*) inelastic plus one neutron stripping transfer couplings; and (*iv*) inelastic, one neutron stripping, and one neutron pickup (full CRC) calculations. It is clear that the couplings to the one neutron transfer channels are quite important to describe the data at the sub-barrier energy region. The full CRC results are in good agreement with the data, except at the region well above the barrier where some hindrance of the data (relative to theory) is observed. Part of the missing yield is related to the fission process which was not measured in the experiment. In reference [19], the fission cross section for the ^{10}B + ^{209}Bi at an incident energy of about 10% above the Coulomb barrier is about 30% of the total fusion.

In [20], ^{9}Be events from the ^{10}B + ^{197}Au reaction were observed. As discussed in that paper, these ^{9}Be events are related to two different processes: the one proton stripping transfer, ^{197}Au(^{10}B, ^{9}Be)^{198}Hg, and the noncapture breakup process, $^{10}\mathrm{B} + {}^{197}\mathrm{Au} \rightarrow {}^{9}\mathrm{Be} + {}^{197}\mathrm{Au} + p$. The total (integrated) cross sections for this process (detection of ^{9}Be) obtained in [20] are presented as yellow squares in Fig. 8. These cross sections were obtained only in two sub-barrier energies. Unfortunately, data for this process could not be obtained with the γ ray method employed in the present work. Therefore, it was not possible to estimate spectroscopic amplitude factors for the one proton stripping transfer and include this channel in the full CRC calculation. As can be observed in Fig. 8, the experimental ^{9}Be cross section is significantly larger than the CF data at this very low energy region.

Now we present a comparison of the experimental fusion cross sections for ^{10}B + ^{197}Au with data for other systems involving the same target nucleus. These data were obtained in [34–40], with projectiles ranging from ^{4}He to ^{48}Ca. In order to remove trivial differences of the fusion cross sections related to the "size" of the system, we adopt the reduced energy and cross section as proposed in [41,42]. These quantities are related to the Wong cross section [43]:

$$\sigma_{\mathrm{Wong}} = \frac{R_B^2 \hbar w}{2E_{\mathrm{c.m.}}} \ln\left\{1 + \exp\left[\frac{2\pi(E_{\mathrm{c.m.}} - V_B)}{\hbar w}\right]\right\}, \quad (3)$$

where R_B, V_B, and $\hbar w$ are the *s*-wave barrier radius, height, and curvature, respectively. We have calculated these parameter values assuming the parameter-free SPP. Defining the adimensional reduced energy and cross section as

$$E_{\mathrm{red}} = \frac{E_{\mathrm{c.m.}} - V_B}{\hbar w}, \quad (4)$$

$$\sigma_{\mathrm{red}} = \frac{2E_{\mathrm{c.m.}}}{R_B^2 \hbar w}\, \sigma_{\mathrm{Wong}}, \quad (5)$$

the Wong formula can be rewritten as

$$\sigma_{\mathrm{UFF}} = \ln[1 + \exp(2\pi E_{\mathrm{red}})]. \quad (6)$$

According to Eq. (3), the Wong cross section clearly depends on the system through its barrier parameter values. On the other hand, the form of Eq. (6) does not depend of the system, since the effects of the barrier parameters are now involved only in Eqs. (4) and (5). Thus, in some papers Eq. (6) is named as the universal fusion function (UFF).

We are interested to compare fusion data for different systems purging trivial effects related to the size of the nuclei. The purpose is to look for differences related to different couplings that affect fusion. At a first glance, Eqs. (4) and (5) could be used to reach this goal, just by exchanging σ_{Wong} by the experimental fusion cross section (σ_{Fus}) in Eq. (5). With this, a comparison of the experimental reduced cross section with the theoretical prediction of Eq. (6) would provide an estimate of the effect of the couplings. Nevertheless, Wong's expression is just an approximation for the quantum calculation of fusion in the context of the barrier penetration model (BPM). This approximation is not good in certain cases [41,42,44]. In order to avoid this problem, we define the experimental reduced fusion cross section as

$$\sigma_{\mathrm{red}} = \frac{2E_{\mathrm{c.m.}}}{R_B^2 \hbar w}\, \sigma_{\mathrm{Fus}} \times \frac{\sigma_{\mathrm{Wong}}}{\sigma_{BPM}}, \quad (7)$$

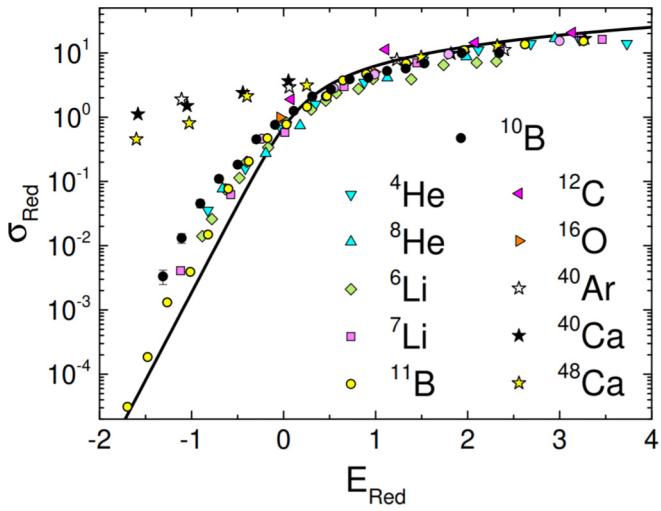

FIG. 9. Experimental reduced fusion cross section as a function of the reduced energy, for several systems involving the same target nucleus: ^{197}Au. The solid lines represent the reduced BPM cross section.

where the factor $\frac{\sigma_{\text{Wong}}}{\sigma_{BPM}}$ represents a correction to the Wong approximation. The BPM cross section is calculated according to [41].

Figure 9 presents experimental reduced fusion cross sections determined from Eq. (7) as a function of the reduced energy calculated from Eq. (4) for several systems involving ^{197}Au as target. The solid lines in the figure correspond to Eq. (6), which in fact represents the reduced BPM cross section.

Due to the stronger coupling, data for very heavy projectiles (^{40}Ar, ^{40}Ca, and ^{48}Ca) present huge enhancement in comparison with the BPM cross sections at sub-barrier energies (note that the barrier height corresponds to $E_{\text{red}} = 0$). On the other hand, all the lighter systems present similar behavior, small enhancement at the sub-barrier region, with exception of the $^{10}\text{B} + ^{197}\text{Au}$ for which the enhancement is somewhat larger. We suggest that this behavior could be due to the effect of the coupling to the one neutron pickup transfer, which is very important for the appropriate description of the fusion process in the case of ^{10}B. In a recent systematical study of optical potential strengths in reactions involving strongly, weakly bound, and exotic nuclei on ^{120}Sn [15] a significant reduction of absorption processes has been identified in the case of ^{10}B, when compared to other weakly bound projectiles (e.g., ^{6,7}Li, ^{9}Be). In the present work, an enhancement of the fusion cross section is obtained for ^{10}B when compared to other weakly bound projectiles, mainly at energies below the barrier. This indicates that fusion is somehow favored for ^{10}B, while peripheral reaction channels, which are connected to strong surface absorption processes, are favored for the other weakly bound nuclei. This behavior seems to be connected to the projectile breakup energy threshold [15].

IV. CONCLUSION

In this work we report the measurement of the different channels contributing to the total fusion cross section for the $^{10}\text{B} + ^{197}\text{Au}$ system at energies below and above the Coulomb barrier using an offline γ-ray spectroscopy method. This method has proven to be very sensitive for almost all channels of the analyzed system. It is worth mentioning that events coming from the incomplete fusion $^{6}\text{Li} + ^{197}\text{Au}$ could not be distinguished experimentally from the yields arising from other processes leading to the same Pb isotopes. Furthermore, cross sections related to the $\alpha + ^{197}$Au incomplete fusion process were experimentally compatible with zero. A similar result was obtained for the $^{10}\text{B} + ^{159}$Tb system [18].

Cross section for the n-pickup obtained by this offline method was compared and found in agreement with the online measurements at below barrier energies. Realistic simulations for this cross sections and the n-stripping were performed.

The data for the total fusion was compared with full CRC calculations, assuming the São Paulo potential as the nuclear interaction. The couplings to the one-neutron transfer channels turned to be important to describe the data at the sub-barrier energies. A good agreement was achieved, except at the region well above the barrier where hindrance of the total fusion cross section can be observed. Part of the missing yield is related to the fission process which was not measured in the experiment.

In addition, the universal fusion function was calculated to compare the behavior of the total fusion cross section with data for other systems with projectiles ranging form ^{4}He to ^{48}Ca over ^{197}Au, showing similar behavior with all the lighter systems except for some enhancement in the region below the barrier. This effect could be due to the importance of the effect of the coupling to the one neutron pickup transfer of this system.

ACKNOWLEDGMENTS

This work was partially supported by Consejo Nacional de Investigaciones Científicas y Técnicas (CONICET, Argentina), through Grant No. PIP00786CO; Fondo para la Investigacin Cientfica y Tecnolgica (FONCYT, Argentina) through Grant no. PICT-2017-4088; Fundação de Amparo à Pesquisa do Estado de São Paulo (FAPESP, Brazil) Proc. Nos. 2018/09998-8, 2019/07767-1, and 2019/05769-7; Conselho Nacional de Desenvolvimento Científico e Tecnológico (CNPq, Brazil) Proc. No 302160/2018-3 and 304056/2019-7, and project INCT-FNA Proc. No. 464898/2014-5; and the Ministry of Science, Innovation and Universities of Spain, through Project No. PGC2018-096994-B-C21.

[1] G. Satchler and W. Love, Phys. Rep. **55**, 183 (1979).
[2] G. Satchler, *Direct Nuclear Reactions* (Clarendon Press, Oxford, 1983).
[3] G. Satchler, Phys. Rep. **199**, 147 (1991).
[4] D. T. Khoa, Nucl. Phys. A **484**, 376 (1988).
[5] M. Brandan and G. Satchler, Nucl. Phys. A **487**, 477 (1988).

[6] M. Brandan and G. Satchler, Phys. Rep. **285**, 143 (1997).

[7] R. J. Glauber, W. E. Brittin, and L. G. Dunhan, *Lectures in Theoretical Physics* (Wiley-Interscience, New York, 1959), Vol. 1, p. 315.

[8] L. F. Canto, P. R. S. Gomes, J. Lubian, L. C. Chamon, and E. Crema, J. Phys. G: Nucl. Part. Phys. **36**, 015109 (2008).

[9] L. Canto, P. Gomes, J. Lubian, L. Chamon, and E. Crema, Nucl. Phys. A **821**, 51 (2009).

[10] G. Satchler, M. Nagarajan, J. Lilley, and I. Thompson, Ann. Phys. (NY) **178**, 110 (1987).

[11] V. A. B. Zagatto, J. Lubian, L. R. Gasques, M. A. G. Alvarez, L. C. Chamon, J. R. B. Oliveira, J. A. Alcántara-Núñez, N. H. Medina, V. Scarduelli, A. Freitas, I. Padron, E. S. Rossi, and J. M. B. Shorto, Phys. Rev. C **95**, 064614 (2017).

[12] D. Heimann, A. Pacheco, O. Capurro, A. Arazi, P. Carnelli, M. Cardona, E. Barbará, J. Niello, J. Figueira, L. Fimiani, D. Hojman, G. Marti, and A. Negri, AIP Conf. Proc. **1423**, 109 (2012).

[13] L. R. Gasques, A. S. Freitas, L. C. Chamon, J. R. B. Oliveira, N. H. Medina, V. Scarduelli, E. S. Rossi, Jr., M. A. G. Alvarez, V. A. B. Zagatto, J. Lubian, G. P. A. Nobre, I. Padron, and B. V. Carlson, Phys. Rev. C **97**, 034629 (2018).

[14] M. A. G. Alvarez, M. Rodríguez-Gallardo, L. R. Gasques, L. C. Chamon, J. R. B. Oliveira, V. Scarduelli, A. S. Freitas, E. S. Rossi, V. A. B. Zagatto, J. Rangel, J. Lubian, and I. Padron, Phys. Rev. C **98**, 024621 (2018).

[15] M. A. G. Alvarez, J. P. Fernández-García, J. L. León-García, M. Rodríguez-Gallardo, L. R. Gasques, L. C. Chamon, V. A. B. Zagatto, A. Lépine-Szily, J. R. B. Oliveira, V. Scarduelli, B. V. Carlson, J. Casal, A. Arazi, D. A. Torres, and F. Ramirez, Phys. Rev. C **100**, 064602 (2019).

[16] D. J. Hinde, M. Dasgupta, B. R. Fulton, C. R. Morton, R. J. Wooliscroft, A. C. Berriman, and K. Hagino, Phys. Rev. Lett. **89**, 272701 (2002).

[17] M. Dasgupta, P. R. S. Gomes, D. J. Hinde, S. B. Moraes, R. M. Anjos, A. C. Berriman, R. D. Butt, N. Carlin, J. Lubian, C. R. Morton, J. O. Newton, and A. Szanto de Toledo, Phys. Rev. C **70**, 024606 (2004).

[18] A. Mukherjee, S. Roy, M. Pradhan, M. S. Sarkar, P. Basu, B. Dasmahapatra, T. Bhattacharya, S. Bhattacharya, S. Basu, A. Chatterjee, V. Tripathi, and S. Kailas, Phys. Lett. B **636**, 91 (2006).

[19] L. R. Gasques, D. J. Hinde, M. Dasgupta, A. Mukherjee, and R. G. Thomas, Phys. Rev. C **79**, 034605 (2009).

[20] L. R. Gasques, L. C. Chamon, A. Lépine-Szily, V. Scarduelli, V. A. B. Zagatto, D. Abriola, A. Arazi, M. A. Cardona, E. de Barbará, J. de Jesús, D. Hojman, G. V. Martí, A. J. Pacheco, D. R. López, M. A. G. Alvarez, J. P. Fernández-García, M. Cubero, L. F. U. Castro, and S. A. Prado, Phys. Rev. C (to be published).

[21] O. B.Tarasov and D. Bazin, Nucl. Instrum. Methods Phys. Res. B **266**, 4657 (2008); A. Gavron, Phys. Rev. C **21**, 230 (1980).

[22] C. Chiara and F. Kondev, Nucl. Data Sheets **111**, 141 (2010).

[23] F. Kondev, Nucl. Data Sheets **105**, 1 (2005).

[24] S. Zhu and F. Kondev, Nucl. Data Sheets **109**, 699 (2008).

[25] F. Kondev, Nucl. Data Sheets **108**, 365 (2007).

[26] F. Kondev and S. Lalkovski, Nucl. Data Sheets **108**, 1471 (2007).

[27] B. Singh, Nucl. Data Sheets **108**, 79 (2007).

[28] X. Huang and M. Kang, Nucl. Data Sheets **133**, 221 (2016).

[29] H. Xiaolong, Nucl. Data Sheets **108**, 1093 (2007).

[30] R. Firestone, Nucl. Data Sheets **108**, 2319 (2007).

[31] See Supplemental Material at http://link.aps.org/supplemental/10.1103/PhysRevC.101.044601 for the values of the measured cross sections.

[32] I. J. Thompson, Comput. Phys. Rep. **7**, 167 (1988).

[33] L. C. Chamon, B. V. Carlson, L. R. Gasques, D. Pereira, C. De Conti, M. A. G. Alvarez, M. S. Hussein, M. A. Cândido Ribeiro, E. S. Rossi, and C. P. Silva, Phys. Rev. C **66**, 014610 (2002).

[34] A. Shrivastava, K. Mahata, V. Nanal, S. K. Pandit, V. V. Parkar, P. C. Rout, N. Dokania, K. Ramachandran, A. Kumar, A. Chatterjee, and S. Kailas, Phys. Rev. C **96**, 034620 (2017).

[35] H. Kurz, E. Jasper, K. Fischer, and F. Hermes, Nucl. Phys. A **168**, 129 (1971).

[36] A. Lemasson, A. Shrivastava, A. Navin, M. Rejmund, N. Keeley, V. Zelevinsky, S. Bhattacharyya, A. Chatterjee, G. de France, B. Jacquot, V. Nanal, R. G. Pillay, R. Raabe, and C. Schmitt, Phys. Rev. Lett. **103**, 232701 (2009).

[37] C. S. Palshetkar, S. Thakur, V. Nanal, A. Shrivastava, N. Dokania, V. Singh, V. V. Parkar, P. C. Rout, R. Palit, R. G. Pillay, S. Bhattacharyya, A. Chatterjee, S. Santra, K. Ramachandran, and N. L. Singh, Phys. Rev. C **89**, 024607 (2014).

[38] S. Baba, K. Hata, S. Ichikawa, T. Sekine, Y. Nagame, A. Yokoyama, M. Shoji, T. Saito, N. Takahashi, H. Baba, and I. Fujiwara, Z. Phys. A **331**, 53 (1988).

[39] C. Ngô, J. Péter, B. Tamain, M. Berlanger, and F. Hanappe, Z. Phys. A **283**, 161 (1977).

[40] A. J. Pacheco, J. O. Fernández Niello, D. E. DiGregorio, M. di Tada, J. E. Testoni, Y. Chan, E. Chávez, S. Gazes, E. Plagnol, and R. G. Stokstad, Phys. Rev. C **45**, 2861 (1992).

[41] L. R. Gasques, L. C. Chamon, D. Pereira, M. A. G. Alvarez, E. S. Rossi, C. P. Silva, and B. V. Carlson, Phys. Rev. C **69**, 034603 (2004).

[42] L. F. Canto, P. R. S. Gomes, J. Lubian, M. S. Hussein, and P. Lotti, Eur. Phys. J. A **50**, 89 (2014).

[43] C. Y. Wong, Phys. Rev. Lett. **31**, 766 (1973).

[44] P. R. S. Gomes, D. R. M. Junior, L. F. Canto, J. Lubian, and P. N. de Faria, Few-Body Syst. **57**, 205 (2016).